

Lattice Instability and Ultralow Lattice Thermal Conductivity of Layered PbIF

N. Yedukondalu,^{*,†,‡} Amir Shafique,[¶] S. C. Rakesh Roshan,^{§,||} Mohamed Barhoumi,[⊥] Rajmohan Muthaiah,[#] Lars Ehm,^{†,‡} John B. Parise,^{†,‡} and Udo Schwingenschlögl^{*,¶}

[†]*Department of Geosciences, Stony Brook University, Stony Brook, New York 11794-2100, USA*

[‡]*Joint Photon Sciences Institute, Stony Brook University, Stony Brook, New York 11790-2100, USA*

[¶]*Applied Physics Program, Physical Science and Engineering Division (PSE), King Abdullah University of Science and Technology (KAUST), Thuwal 23955-6900, Saudi Arabia*

[§]*Rajiv Gandhi University of Knowledge Technologies, Basar, Telangana-504107, India*

^{||}*Department of Physics, National Institute of Technology-Warangal, Telangana, India*

[⊥]*Laboratoire de la Matière Condensée et des Nanosciences (LMCN), Université de Monastir, Département de Physique, Faculté des Sciences de Monastir, Avenue de le environnement, 5019 Monastir, Tunisia*

[#]*School of Aerospace and Mechanical Engineering, University of Oklahoma, Norman, OK 73019, USA*

E-mail: nykondalu@gmail.com; udo.schwingenschlogl@kaust.edu.sa

Abstract

Understanding the interplay between various design strategies (for instance, bonding heterogeneity and lone pair induced anharmonicity) to achieve ultralow lattice thermal conductivity (κ_l) is indispensable for discovering novel functional materials for thermal energy applications. In the present study, we investigate layered PbXF (X = Cl, Br, I), which offers bonding heterogeneity through the layered crystal structure, anharmonicity through the Pb²⁺ 6s² lone pair, and phonon softening through the mass difference between F and Pb/X. The weak inter-layer van der Waals bonding and the strong intra-layer ionic bonding with partial covalent bonding result in a significant bonding heterogeneity and a poor phonon transport in the out-of-plane direction. Large average Grüneisen parameters (≥ 2.5) demonstrate strong anharmonicity. The computed phonon dispersions show flat bands, which suggest short phonon lifetimes, especially for PbIF. Enhanced Born effective charges are due to cross-band-gap hybridization. PbIF shows lattice instability at a small volume expansion of 0.1%. The κ_l values obtained by the two channel transport model are 20-50% higher than those obtained by solving the Boltzmann transport equation. Overall, ultralow κ_l values are found at 300 K, especially for PbIF. We propose that the interplay of bonding heterogeneity, lone pair induced anharmonicity, and constituent elements with high mass difference aids the design of low κ_l materials for thermal energy applications.

Keywords: Layered structure, lattice dynamics, phonon transport, bonding heterogeneity, lattice instability.

Introduction

The discovery and design of materials with ultralow lattice thermal conductivity (κ_l) receive tremendous research interest¹ because of potential applications in energy conversion technology. Additionally, (ultra)low κ_l materials with wide band gaps have promising applications in thermal barrier coatings.^{2,3} Ultralow κ_l materials with narrow band gaps are suitable for thermoelectric applications.⁴⁻⁸ Several strategies^{9,10} have been proposed to design ultralow κ_l materials including resonant bonding,¹¹ rattling,¹²⁻¹⁵ cation disorder,¹⁶ bonding heterogeneity,¹⁷⁻¹⁹ and lone pair induced anharmonicity.²⁰⁻²² Combining two or more of these in one material suppresses κ_l effectively. For instance, a lone pair enhances the anharmonicity, while bonding heterogeneity results in anisotropic κ_l with poor phonon transport along the weak bonding (soft) lattice direction. Materials with lone pair cation(s) (In^+ , Tl^+ , Sn^{+2} , Pb^{+2} , Bi^{+3} , Sb^{+3} , etc.)^{12,15,17,22} can exhibit enhanced Born effective charges (BECs) due to cross-band-gap hybridization,^{23,24} causing large splitting between the longitudinal and transverse optical modes and bringing the lattice close to instability.^{23,25-27}

Recently, wide band gap layered semiconductors receive great attention due to potential applications in electronics and optoelectronics in the green and blue wavelength regions.²⁸ In particular, PbClF-type (matlockite) materials attract interest because of their applications in photo-detectors and optoelectronic devices.²⁹⁻³² Barhoumi et al.³³ have investigated the electronic and vibrational properties of several PbClF-type two-dimensional (2D) materials for possible utilization in optoelectronic devices. Tan et al.³⁴ have synthesized 2D lead halides and mixed halofluorides to develop low-cost, high-sensitivity, low-noise, and flexible ultraviolet photodetectors. Understanding the finite temperature lattice dynamics and phonon transport is critically important for deploying PbXF ($X = \text{Cl}, \text{Br}, \text{I}$) as low κ_l materials. However, only few studies have focused on PbClF-type materials such as 2D-SrBrF³⁵ and the bulk crystals CaClF and SrClF.³⁶

PbXF ($X = \text{Cl}, \text{Br}, \text{I}$) crystallizes in the tetragonal space group $P4/nmm$ with two formula units in the primitive cell.³⁷ F occupies the Wyckoff position 2a ($3/4, 1/4, 0$) and

Pb and X occupy the Wyckoff position 2c ($1/4, 1/4, v/u$). The Pb^{2+} cations have $6s^2$ lone pairs. The structure consists of X-Pb-F-F-Pb-X layers, with strong intra-layer ionic bonding (ab -plane), which are connected in the c -direction by weak inter-layer van der Waals (vdW) bonding, similar to MXF ($M = \text{Ca, Sr, Ba}$ and $X = \text{Cl, Br, I}$) at ambient conditions.^{38,39} Panels a and b of Figure 1 show the matlockite structure of PbIF. The combination of intra-layer ionic bonding with inter-layer vdW bonding results in bonding heterogeneity and thus in anisotropic phonon transport, directly affecting the phonon group velocities. As there are no studies available that explore the potential of PbXF ($X = \text{Cl, Br, I}$) in optoelectronic devices and thermal energy management, we systematically investigate the electronic structure, anharmonic lattice dynamics, and phonon transport.

Computational details and methodology

First principles calculations are performed using the Vienna ab initio simulation package (VASP).⁴⁰ The electron-electron interaction is treated by the PBEsol exchange-correlation functional within the generalized gradient approximation and the electron-ion interaction by the projector augmented wave pseudopotential approach. The following valence electrons are considered: F $2s^2, 2p^5$, Cl $3s^2, 3p^5$, Br $4s^2, 4p^5$, I $5s^2, 5p^5$, and Pb $5d^{10}, 6s^2, 6p^2$. For the structural optimization and computation of the 2nd order elastic constants an energy cutoff of 600 eV is used for the plane wave basis and a spacing of $2\pi \times 0.025 \text{ \AA}^{-1}$ for the k-mesh of the Brillouin zone integration. Electronic structure calculations are performed using the Tran-Blaha modified Becke-Johnson (TB-mBJ)⁴¹ potential as implemented in WIEN2k,⁴² and the Heyd-Scuseria-Ernzerhof (HSE)⁴³ functional as implemented in VASP.⁴⁰

The finite temperature lattice dynamics and thermal conductivity of PbXF ($X = \text{Cl, Br, I}$) are studied using the temperature dependent effective potential (TDEP) method.⁴⁴ To compute the harmonic (second order) and anharmonic (third order) inter-atomic force constants (IFCs) at 300 K we perform ab initio molecular dynamics (AIMD) simulations using

VASP, comprising 5000 steps of 1 fs (5 ps total duration) with the temperature controlled by a Nosé-Hoover thermostat. A $4 \times 4 \times 2$ (192 atoms) supercell is used and only the Γ -point is considered in the Brillouin zone integration. For calculating the second and third order IFCs, interactions up to 9th nearest neighbours are included to ensure convergence of the phonon dispersion and lattice thermal conductivity. TDEP includes finite temperature effects on the second and third order IFCs, which are critical for highly anharmonic low κ_l materials. The lattice thermal conductivity is calculated by iteratively solving the Boltzmann transport equation (BTE), including three-phonon and isotope (natural distribution) scattering on a $19 \times 19 \times 19$ q-mesh using both TDEP⁴⁴ and ShengBTE.⁴⁵ In the case of ShengBTE the finite displacement method with a $3 \times 3 \times 2$ supercell is employed to calculate the second and third order IFCs by Phonopy⁴⁶ and the thirdorder.py script,⁴⁷ respectively.

Results and Discussion

Crystal structure, bonding, and elastic properties

Since the matlockite structure of PbXF ($X = \text{Cl, Br, I}$) is layered (Figure 1a,b), we optimize it using the PBEsol, DFT-D2, and non-local optB88-vdW and optB86b-vdW methods to capture the vdW interaction. The experimental volume is well reproduced by the PBEsol and optB86b-vdW methods (Supporting Information Tables S1 & S2). We choose the equilibrium structure obtained by the PBEsol functional to compute the Bader charges, elastic properties, lattice dynamics, and thermal conductivity. The calculated electron localization function (ELF) shows a strong intra-layer ionic bonding with partial covalent bonding along with stereochemical activity of the Pb^{2+} $6s^2$ lone pair (Figure 1c,d). To understand the bonding nature quantitatively, we calculate the Bader charges of the Pb, F, and X ions, finding that the two valence electrons of the Pb^{2+} cation are not completely transferred to the F and X anions (Table 1), confirming a mixed ionic and covalent bonding character. The charge transfer from Pb to Cl (-0.7), Br (-0.6), and I (-0.5) decreases with the size of the anion,

indicating that the covalent contribution to the bonding increases, while the bonding between Pb and F is mainly ionic. The bonding character of PbXF (X = Cl, Br, I) thus changes with the size (electronegativity) of the X anion.

The elastic constants of crystalline solids provide insights into the bonding strengths, mechanical properties, and stability. The elastic constants obtained at the PBEsol equilibrium volume and at the experimental volume, as presented in Table 2, agree with the available experimental results as well as with the results of previous calculations.⁴⁸ Due to the tetragonal space group, the elastic tensor has six independent constants (C_{11} , C_{33} , C_{12} , C_{13} , C_{44} , and C_{66}). The computed values fulfill the Born's stability criteria, $C_{11} > 0$, $C_{33} > 0$, $C_{44} > 0$, $C_{66} > 0$, $(C_{11}-C_{12}) > 0$, $(C_{11} + C_{33} - 2C_{13}) > 0$, and $[2(C_{11}+C_{12}) + C_{33}+4C_{13}] > 0$, indicating mechanical stability at ambient pressure. As Table 2 shows $C_{33} < C_{11}$ for all three materials, the lattice is softer in the c -direction than in the a -direction. This is due to the weak vdW interaction between the X-Pb-F-F-Pb-X layers stacked along the c -direction. Moreover, we find $C_{13} < C_{12}$ and $C_{44} < C_{66}$, demonstrating substantial elastic anisotropy, which also originates from the layered crystal structure. Similar trends have been reported for the ultralow κ_l materials BiCuChO (Ch = S, Se, Te), which crystallize in the same space group ($P4/nmm$) and realize a layered ZrSiCuAs-type structure.⁴⁹

We calculate the bulk (B) and shear (G) moduli from the elastic constants using the Voigt-Reuss-Hill (VRH) approximation³⁸ and then calculate Young's modulus (E) from the obtained B and G values. The calculated B, G, and E values decrease from PbClF to PbBrF to PbIF, pointing to a weakening of the interatomic interactions for increasing size of the X anion (Table 3). Low values indicate that the materials are easily deformed by mechanical stress. Usually, soft materials with heavy elements show low optical phonon frequencies, which enhances the coupling with the acoustic modes, thus enhancing the phonon scattering and lowering κ_l . Using the obtained B and G values, the longitudinal (v_l) and transverse (v_t) sound velocities are calculated as $\rho v_l^2 = B + \frac{4G}{3}$ and $\rho v_t^2 = G$, respectively, where ρ is the mass density. The Debye temperature (θ) can be estimated from the average sound velocity

(v_m) as

$$\theta = \frac{\hbar}{k_B} (6\pi^2 n)^{\frac{1}{3}} v_m, \quad (1)$$

where \hbar , k_B , and n are the reduced Planck constant, Boltzmann constant, and number of atoms per unit cell, respectively. From the obtained v_l and v_t values, v_m is calculated from the relation $\frac{3}{v_m^3} = \frac{1}{v_l^3} + \frac{2}{v_t^3}$. The presence of low lying optical phonons results in softening of the acoustic phonons, which generates low sound velocities and therefore low θ ($\propto v_m$). According to the Slack theory, a low θ value is an indication of low κ_l . The calculated v_l , v_t , v_m , and θ values decrease from PbClF to PbBrF to PbIF and a similar trend thus is expected for κ_l . The mechanical properties of the investigated materials are summarized in Table 3.

Born effective charges and cross-band-gap hybridization

Owing to the polar nature of PbXF (X = Cl, Br, I), long-range dipole-dipole interaction produces a splitting between the longitudinal optical (LO) and transverse optical (TO) phonons, known as LO-TO splitting. The calculated BECs, which represent the dynamic electron density associated with the covalent bonding, are presented in Table 4. With decreasing electronegativity of the halogen anion, F to Cl to Br to I, the ionic character of the Pb-X bond decreases, resulting in enhanced in-plane BECs consistent with previously observed trends in layered α -PbO⁵⁰ and BiCuChO (Ch = S, Se, Te),⁴⁹ which crystallize in the same ($P4/nmm$) space group. The in-plane BECs are close to double of the formal charges (+2 for Pb and -1 for F, Cl, Br, I) due to the Pb²⁺ 6s² lone pair. Similarly enhanced BECs have been reported for lone pair containing In, Tl, Pb, and Bi halides,^{23,24} in which the outermost cation s -states are fully occupied and the states at the conduction band minimum are mainly derived from the spatially more extended cation p -states. This causes a significant cross-band-gap hybridization between the cation p - and halogen p -states.^{23,24}

The electronic band gaps obtained without and with spin-orbit coupling (SOC) are pre-

sented in Table 5. While the PBE functional underestimates the band gap for semiconductors and insulators, the values obtained by the HSE functional and TB-mBJ potential agree with each other. The value of 4.8 (4.7) eV calculated without (with) SOC for PbClF slightly underestimates the 5.0 eV obtained by the computationally expensive GW approach and the 5.2 eV obtained by reflection spectroscopy.⁵¹ The band gap decreases from PbClF to PbBrF to PbIF due to shifts of the cation p -states for increasing size of the X anion.

In general, the obtained band structures are similar to those of previous calculations.⁵¹⁻⁵³ As shown in Figure 2, the valence band can be broadly divided into three regions, which are well separated for PbIF in contrast to PbClF and PbBrF. This trend can be attributed to the increasing electronegativity difference between F (3.98, Pauling scale) and Cl (3.16), Br (2.96), and I (2.66). As illustrated in Figure 2, the valence band edge is dominated by the X p -states with minor contributions of the Pb s -states and F p -states, the middle region is dominated by the F p -states with small contributions of the X p -states, and the lower region arises from strongly hybridized Pb s -states and F p -states. The dispersive nature of the valence band is the result of hybridization between the fully occupied Pb s -states and the X and F p -states. The conduction band is dominated by the nominally unoccupied Pb p -states, which hybridize with the X and F p -states. This gives rise to a considerable cross-band-gap hybridization and, thus, enhancement of the BECs.

Our results also provide insight into the activity of the $\text{Pb}^{2+} 6s^2$ lone pair. When the lone pair is stereochemically (in)active, the projected density of states (PDOS) shows that the occupied cation s -states are (narrow) broad and (largely unmixed) well mixed with the anion p -states, with intermediate unoccupied cation p -states.⁵⁴ In the metal chalcogenides AQ (A = Ge, Sn, Pb and Q = S, Se, Te), which contain lone pair cations, the strength of the stereochemical activity decreases for increasing size of the chalcogen atom due to separation between the cation s -states and anion p -states in the valence band. As shown in Figure 2, the occupied $\text{Pb}^{2+} s$ -states are narrow and become increasingly separated from the anion (F^- and X^-) p -states from PbClF to PbBrF to PbIF, developing a pseudo gap. This indicates

that the stereochemical activity decreases for increasing size of the X anion, similar to the behavior observed for AQ (A = Ge, Sn, Pb and Q = S, Se, Te).⁵⁴

Anharmonic lattice dynamics and thermal conductivity

As the phonon frequencies (Raman and IR) at the Γ -point are vital to understand the lattice dynamics and phonon transport, they have been extensively studied for MXF (M = Ca, Sr, Ba and X = Cl, Br, I).⁵⁵⁻⁵⁹ These materials possess six atoms in the unit cell, resulting in a total of 18 (3 acoustic and 15 optical) phonon modes. According to group theory, the symmetry decomposition of the Γ -point phonons for the $P4/nmm$ space group is $\Gamma_{18} = 6E_g \oplus 2A_{1g} \oplus B_{1g} \oplus 6E_u \oplus 3A_{2u}$, with six Raman active (A_{1g} , B_{1g} , E_g) and four IR active (A_{2u} , E_u) modes, where E_g and E_u are doubly degenerate (Figures S1 & S2).

The phonon dispersions and densities of states of PbXF (X = Cl, Br, I) in Figure 3 (calculated including the third order IFCs) show no imaginary frequencies, demonstrating dynamical stability at 300 K. The low-(high-)frequency phonons are mainly due to vibrations of the Pb, I, and Br (F and Cl) atoms. The phonon bands are more dispersive for PbClF than PbBrF and PbIF due to the smaller mass difference between F and Cl as compared to that between F and Br/I, which leads to a phonon band gap in the cases of PbBrF and PbIF as previously reported for MQ (M = Ca, Sr, Ba and Q = S, Se, Te).⁶⁰ In the low frequency region, the phonon density of states (Figure 3) is due to overlapping acoustic and low lying optical phonons mainly involving vibrations of the Pb atoms (with contributions of I only in the case of PbIF). The vibrational frequencies of the Cl, Br, and I atoms show a red-shift from PbClF to PbBrF to PbIF due to the increasing mass difference to F. The red-shift is associated with an increasing LO-TO splitting that reduces the dispersions of the phonon bands below 3 THz from PbClF to PbBrF to PbIF (Figure 3). This substantial softening of the acoustic phonons increases the scattering phase space and aids the suppression of κ_l (especially for PbIF), similar to the previously observed behavior in layered BiCuSeO.⁶¹

Figure 4 shows κ_l as a function of temperature. Using TDEP (ShengBTE) at 300 K,

ultralow κ_l values (in $\text{Wm}^{-1}\text{K}^{-1}$) are predicted in the c -direction (0.73 (0.98) for PbClF; 0.42 (0.55) for PbBrF; 0.11 (0.16) for PbIF) and significantly higher values in the a -direction (1.44 (1.47) for PbClF; 0.93 (0.90) for PbBrF; 0.61 (0.84) for PbIF). This strong anisotropy of κ_l originates from the bonding heterogeneity which results in $v_t < v_l$ (Table 3). The calculated average κ_l values at 300 K are 1.20 (1.31), 0.76 (0.78), and 0.45 (0.61) $\text{Wm}^{-1}\text{K}^{-1}$ for PbClF, PbBrF, and PbIF, respectively. PbXF (X = Cl, Br, I) shows ultralow κ_l values in the c -direction in the whole temperature range from 200 to 800 K. Accordingly, the c -direction gives only minor contributions to the cumulative κ_l (Figure 5a). About 70% of κ_l is due to phonons below 2.1 THz for PbClF, 2.2 THz for PbBrF, and 1.85 THz for PbIF (Figure 5b). While the optical phonons contribute significantly to κ_l , the low dispersions of the acoustic and low lying optical phonon bands result in the ultralow κ_l values.

We study the phonon group velocities, lifetimes, and mean free path as functions of frequency at 300 K. For a solid material we have

$$\kappa_l = \frac{1}{3} \int C(\omega) v_g^2(\omega) \tau(\omega) d\omega, \quad (2)$$

where $C(\omega)$ is the spectral volumetric specific heat, $v_g(\omega)$ is the phonon group velocity, and $\tau(\omega)$ is the phonon lifetime. The calculated phonon group velocities (Table 6) are smaller in the c -direction (Γ -Z) than in the a -direction (Γ -X), as the weak inter-layer vdW bonding prevents phonon transport in the c -direction, and they are lower for PbIF than for PbClF and PbBrF (Figure 6). We find that the flat phonon bands dominated by vibrations of the Pb and Br/I atoms are associated with relatively low phonon lifetimes (Figure 7), which is due to enhanced three-phonon scattering.⁶¹ PbIF shows shorter lifetimes of the acoustic and low lying optical phonons than PbBrF and PbClF, hence realizing the lowest κ_l values. The anharmonicity due to the $\text{Pb}^{2+} 6s^2$ lone pair can be quantified by the dimensionless Grüneisen parameter (γ). High γ values of both the acoustic and low lying optical phonons represent a strongly anharmonic behavior (Figure 8). The calculated average γ values are 2.67, 2.84,

and 2.50 for PbClF, PbBrF, and PbIF, respectively, being higher than in anharmonic lead chalcogenides such as PbS (2.46), PbSe (2.66), and PbTe (1.49).⁶²

The obtained high BECs (Table 4) due to the cross-band-gap hybridization between the Pb p -states and X p -states suggest that the materials are close to lattice instability. We therefore calculate the phonon dispersions for small (equilibrium) volume expansions from 0.1 to 4%. PbClF, PbBrF, and PbIF become dynamically unstable at volume expansions of 4%, 2%, and 0.1%, respectively (Figure 9). The fact that PbIF becomes dynamically unstable already for a small volume expansion points to proximity to immediate lattice instability, thus resulting in ultralow κ_l .

Considerable portions of the calculated phonon mean free paths are found to fall below the Ioffe-Regel limit (Figure 10), which implies that these phonons are ill-defined and the BTE, therefore may be insufficient to reproduce the experimental κ_l values. To address the presence of ill-defined phonons along with well-defined phonons, we use a phenomenological model that describes the phonon transport in two channels: lattice phonons propagating as wave packets (κ_{BTE}) and hopping among uncorrelated localized oscillators (κ_{hop}).⁶³ Thus, $\kappa_l = \kappa_{BTE} + \kappa_{hop}$. The Cahill-Watson-Pohl model provides

$$\kappa_{hop} = \left(\frac{\pi}{6}\right)^{1/3} k_B n^{2/3} \sum_i v_i \left(\frac{T}{\theta_i}\right)^2 \int_0^{\theta_i/T} \frac{x^3 e^x}{(e^x - 1)^2} dx, \quad (3)$$

where v_i and θ_i are the phonon velocity, and Debye temperature of the acoustic branch i , respectively (calculated using eq 1). The two channel transport model reproduces the experimental κ_l values for various ultralow κ_l materials such as Tl₃VSe₄,⁶³ Tl₃VS₄,⁶⁴ Tl₃TaS₄,⁶⁴ TlInTe₂,⁶⁵ and TlAgTe.⁶⁶ At 300 K, the calculated κ_l values are 1.66, 1.14, and 0.90 Wm⁻¹K⁻¹ for PbClF, PbBrF, and PbIF, respectively, exceeding those obtained using Sheng-BTE by iteratively solving the BTE by 20-50% (Figures 4 & 10b), which demonstrates that the two channel model is essential to calculate κ_l accurately for materials with ultralow κ_l , consistent with previous reports.⁶³⁻⁶⁶ For instance, the κ_l value calculated by the BTE is

0.158⁶³ (0.17⁶⁶) $\text{Wm}^{-1}\text{K}^{-1}$ and that calculated by the two channel model is 0.368⁶³ (0.43⁶⁶) $\text{Wm}^{-1}\text{K}^{-1}$ for Tl_3VSe_4 (TlAgTe),^{63,67} being comparable with the experimental value of 0.3 ± 0.05 (0.44) $\text{Wm}^{-1}\text{K}^{-1}$.

Conclusions

We have systematically investigated the chemical bonding, elastic properties, electronic properties, lattice dynamics, and phonon transport of PbXF ($X = \text{Cl, Br, I}$) using a combination of density functional theory, Boltzmann transport theory, and a two channel transport model. The obtained low elastic moduli (B, G, and E) and high compressibility suggest that the materials are comparably soft, especially PbIF . Low sound velocities and Debye temperatures are indicative of low κ_l values. Enhanced BECs due to cross-band-gap hybridization bring the materials close to lattice instability. In particular, PbIF becomes instable at 0.1% volume expansion. The computed phonon frequencies show a red-shift for increasing size of the X anion and a large mass difference between F and Pb/X opens up a phonon band gap in PbBrF and PbIF . The layered crystal structure (bonding heterogeneity) results in low phonon group velocities and low phonon transport in the out-of-plane direction. Large γ values (> 2.5) are indicative of a strong anharmonicity. Low dispersions of the low lying optical phonons result in enhanced phonon scattering, which causes a reduction of the phonon lifetimes, especially in PbIF . The κ_l values obtained by solving the BTE using ShengBTE are 1.31, 0.78, and 0.61 $\text{Wm}^{-1}\text{K}^{-1}$ at 300 K for PbClF , PbBrF , and PbIF , respectively, while those obtained by the two channel model are 1.66, 1.14, and 0.90 $\text{Wm}^{-1}\text{K}^{-1}$ (20-50% higher). Overall, the interplay between bonding heterogeneity, lone pair induced anharmonicity, and the high mass differences between F and Pb/I results in softening of the acoustic and low lying optical phonons and causes the ultralow κ_l of PbIF . Our study demonstrates that a material should possess bonding heterogeneity, one or more lone pair containing cations, and high mass differences to achieve ultralow κ_l values, which is critically important to design

functional materials for future thermal energy applications.

Supporting Information

Eigenvectors of the acoustic and optical phonon modes of PbIF (Figures S1 & S2) and ground state structural properties (Tables S1 & S2). (PDF)

Acknowledgments

N.Y. thanks the Stony Brook Research Computing and Cyberinfrastructure as well as the Institute for Advanced Computational Science at Stony Brook University for access to the high-performance SeaWulf computing system, which was made possible by a National Science Foundation grant (1531492). The research reported in this publication was supported by funding from King Abdullah University of Science and Technology (KAUST). S.C.R.R. thanks Rajiv Gandhi University of Knowledge Technologies (RGUKT) Basar for providing computational facilities.

References

- (1) Juneja, R.; Yumnam, G.; Satsangi, S.; Singh, A. K. Coupling the High-Throughput Property Map to Machine Learning for Predicting Lattice Thermal Conductivity. *Chem. Mater.* **2019**, *31*, 5145–5151.
- (2) Moteb, A.; Chen, K. Modelling and Evaluating Thermal Conductivity of Porous Thermal Barrier Coatings at Elevated Temperatures. *Ceram. Int.* **2020**, *46*, 21939–21957.
- (3) Liu, Y.; Jia, D.; Zhou, Y.; Zhou, Y.; Zhao, J.; Li, Q.; Liu, B. Discovery of ABO₄ Scheelites with the Extra Low Thermal Conductivity Through High-Throughput Calculations. *J. Materiomics* **2020**, *6*, 702–711.

- (4) Sajjad, M.; Singh, N.; Sattar, S.; De Wolf, S.; Schwingenschlögl, U. Ultralow Lattice Thermal Conductivity and Thermoelectric Properties of Monolayer Tl_2O . *ACS Appl. Energy Mater.* **2019**, *2*, 3004–3008.
- (5) Guo, M.; Guo, F.; Zhu, J.; Yin, L.; Zhang, Q.; Cai, W.; Sui, J. Achieving High Thermoelectric Performance in Rare-Earth Element-Free CaMg_2Bi_2 with High Carrier Mobility and Ultralow Lattice Thermal Conductivity. *Research* **2020**, *2020*, 5016564.
- (6) Sharma, S.; Shafique, A.; Schwingenschlögl, U. Monolayer Ag_2S : Ultralow Lattice Thermal Conductivity and Excellent Thermoelectric Performance. *ACS Appl. Energy Mater.* **2020**, *3*, 10147–10153.
- (7) Wu, Y. Y.; Zhu, X. L.; Yang, H. Y.; Wang, Z. G.; Li, Y. H.; Wang, B. T. First Principles Calculations on the Thermoelectric Properties of Bulk Au_2S with Ultra-Low Lattice Thermal Conductivity. *Chin. Phys. B.* **2020**, *29*, 087202.
- (8) Osei-Agyemang, E.; Adu, C. E.; Balasubramanian, G. Ultralow Lattice Thermal Conductivity of Chalcogenide Perovskite CaZrSe_3 Contributes to High Thermoelectric Figure of Merit. *NPJ Comput. Mater.* **2019**, *5*, 116.
- (9) Jana, M. K.; Biswas, K. Crystalline Solids with Intrinsically Low Lattice Thermal Conductivity for Thermoelectric Energy Conversion. *ACS Energy Lett.* **2018**, *3*, 1315–1324.
- (10) Dutta, M.; Sarkar, D.; Biswas, K. Intrinsically Ultralow Thermal Conductive Inorganic Solids for High Thermoelectric Performance. *Chem. Commun.* **2021**, *57*, 4751–4767.
- (11) Lee, S.; Esfarjani, K.; Luo, T.; Zhou, J.; Tian, Z.; Chen, G. Resonant Bonding Leads to Low Lattice Thermal Conductivity. *Nat. Commun.* **2014**, *5*, 3525.
- (12) Jana, M. K.; Pal, K.; Warankar, A.; Mandal, P.; Waghmare, U. V.; Biswas, K. Intrinsic

- Rattler-Induced Low Thermal Conductivity in Zintl Type TlInTe_2 . *J. Am. Chem. Soc.* **2017**, *139*, 4350–4353.
- (13) Dutta, M.; Samanta, M.; Ghosh, T.; Voneshen, D. J.; Biswas, K. Evidence of Highly Anharmonic Soft Lattice Vibrations in a Zintl Rattler. *Angew. Chem. Int.* **2021**, *60*, 4259–4265.
- (14) Bhui, A.; Dutta, M.; Mukherjee, M.; Rana, K. S.; Singh, A. K.; Soni, A.; Biswas, K. Ultralow Thermal Conductivity in Earth-Abundant $\text{Cu}_{1.6}\text{Bi}_{4.8}\text{S}_8$: Anharmonic Rattling of Interstitial Cu. *Chem. Mater.* **2021**, *33*, 2993–3001.
- (15) Juneja, R.; Singh, A. K. Rattling-Induced Ultralow Thermal Conductivity Leading to Exceptional Thermoelectric Performance in AgIn_5S_8 . *ACS Appl. Mater. Interfaces* **2019**, *11*, 33894–33900.
- (16) Qiu, W.; Xi, L.; Wei, P.; Ke, X.; Yang, J.; Zhang, W. Part-Crystalline Part-Liquid State and Rattling-Like Thermal Damping in Materials with Chemical-Bond Hierarchy. *Proc. Natl. Acad. Sci. U.S.A.* **2014**, *111*, 15031–15035.
- (17) Dutta, M.; Pal, K.; Waghmare, U. V.; Biswas, K. Bonding Heterogeneity and Lone Pair Induced Anharmonicity Resulted in Ultralow Thermal Conductivity and Promising Thermoelectric Properties in n-Type AgPbBiSe_3 . *Chem. Sci.* **2019**, *10*, 4905–4913.
- (18) Pal, K.; Xia, Y.; He, J.; Wolverton, C. High Thermoelectric Performance in BaAgYTe_3 Via Low Lattice Thermal Conductivity Induced by Bonding Heterogeneity. *Phys. Rev. Mater.* **2019**, *3*, 085402.
- (19) Mukherjee, M.; Singh, A. K. Strong Chemical Bond Hierarchy Leading to Exceptionally High Thermoelectric Figure of Merit in Oxychalcogenide AgBiTeO . *ACS Appl. Energy Mater.* **2020**, *12*, 8280–8287.

- (20) Skoug, E. J.; Morelli, D. T. Role of Lone-Pair Electrons in Producing Minimum Thermal Conductivity in Nitrogen-Group Chalcogenide Compounds. *Phys. Rev. Lett.* **2011**, *107*, 235901.
- (21) Chang, C.; Zhao, L.-D. Anharmonicity and Low Thermal Conductivity in Thermoelectrics. *Mater. Today Phys.* **2018**, *4*, 50–57.
- (22) Rathore, E.; Juneja, R.; Culver, S. P.; Minafra, N.; Singh, A. K.; Zeier, W. G.; Biswas, K. Origin of Ultralow Thermal Conductivity in n-Type Cubic Bulk AgBiS₂: Soft Ag Vibrations and Local Structural Distortion Induced by the Bi 6s² Lone Pair. *Chem. Mater.* **2019**, *31*, 2106–2113.
- (23) Du, M.-H.; Singh, D. J. Enhanced Born Charge and Proximity to Ferroelectricity in Thallium Halides. *Phys. Rev. B* **2010**, *81*, 144114.
- (24) Du, M.-H.; Singh, D. J. Enhanced Born Charges in III-VII, IV-VII₂, and V-VII₃ Compounds. *Phys. Rev. B* **2010**, *82*, 045203.
- (25) Tachibana, M.; Kolodiaznyy, T.; Takayama-Muromachi, E. Thermal Conductivity of Perovskite Ferroelectrics. *Appl. Phys. Lett.* **2008**, *93*, 092902.
- (26) Fu, Y.; Singh, D. J. Thermal Conductivity of Perovskite KTaO₃ and PbTiO₃ from First Principles. *Phys. Rev. Mater.* **2018**, *2*, 094408.
- (27) Banik, A.; Ghosh, T.; Arora, R.; Dutta, M.; Pandey, J.; Acharya, S.; Soni, A.; Waghmare, U. V.; Biswas, K. Engineering Ferroelectric Instability to Achieve Ultralow Thermal Conductivity and High Thermoelectric Performance in Sn_{1-x}Ge_xTe. *Energy Environ. Sci.* **2019**, *12*, 589–595.
- (28) Lu, Y.; Warner, J. H. Synthesis and Applications of Wide Bandgap 2D Layered Semiconductors Reaching the Green and Blue Wavelengths. *ACS Appl. Electron. Mater.* **2020**, *2*, 1777–1814.

- (29) Chen, J.; Shen, D.; Ren, G.; Mao, R.; Yin, Z. A High-Density Inorganic Scintillator: Lead Fluoride Chloride. *J. Phys. D: Appl. Phys.* **2004**, *37*, 938–941.
- (30) Manjunath, K.; Servottam, S.; Soni, A.; Rao, C. N. R. A Study of Two-Dimensional PbFCl and BaFCl. *Bull. Mater. Sci.* **2020**, *43*, 312.
- (31) Barhoumi, M.; Said, M. Electronic and Optical Properties of PbFCl and PbFI Monolayers Using Density Functional Theory and Beyond. *Mater. Chem. Phys.* **2020**, *252*, 123233.
- (32) Ye, X.-J.; Zhu, Z.-X.; Meng, L.; Liu, C.-S. Two-dimensional CaFCl: Ultra-Wide Bandgap, Strong Interlayer Quantum Confinement, and n-Type Doping. *Phys. Chem. Chem. Phys.* **2020**, *22*, 17213–17220.
- (33) Barhoumi, M.; Abboud, A.; Debbichi, L.; Said, M.; Björkman, T.; Rocca, D.; Lebègue, S. Electronic Properties of Several Two Dimensional Halides from Ab Initio Calculations. *Beilstein J. Nanotechnol.* **2019**, *10*, 823–832.
- (34) Tan, M.; Hu, C.; Lan, Y.; Khan, J.; Deng, H.; Yang, X.; Wang, P.; Yu, X.; Lai, J.; Song, H. 2D Lead Dihalides for High-Performance Ultraviolet Photodetectors and Their Detection Mechanism Investigation. *Small* **2017**, *13*, 1702024.
- (35) Tan, J.; Hao, Q.-D.; Zeng, Z.-Y.; Chen, X.-R.; Geng, H.-Y. First-Principles Study of Structural, Electronic, and Thermal Conductivity Properties of Monolayer SrFBr. *J Phys. Chem. Solids* **2021**, *153*, 109956.
- (36) Kunduru, L.; Yedukondalu, N.; Roshan, S. C. R.; Sripada, S.; Sainath, M.; Ehm, L.; Parise, J. B. Pressure-Induced Martensitic Phase Transition and Low Lattice Thermal Conductivity of SrClF. *J. Phys. Chem. C* **2021**, *125*, 17261–17270.
- (37) Flahaut, J. Les Structures Type PbFCl (EOI) Et Type Anti-Fe₂As (C38) Des Compos Ternaires Á Deux Anions MXY. *J. Solid State Chem.* **1974**, *9*, 124–131.

- (38) Yedukondalu, N.; Babu, K. R.; Bheemalingam, C.; Singh, D. J.; Vaitheeswaran, G.; Kanchana, V. Electronic Structure, Optical Properties, and Bonding in Alkaline-Earth Halofluoride Scintillators: BaClF, BaBrF, and BaIF. *Phys. Rev. B* **2011**, *83*, 165117.
- (39) Kanchana, V.; Yedukondalu, N.; Vaitheeswaran, G. Structural, Elastic, Electronic and Optical Properties of Layered Alkaline-Earth Halofluoride Scintillators. *Philos. Mag.* **2013**, *93*, 3563–3575.
- (40) Kresse, G.; Furthmüller, J. Efficient Iterative Schemes for Ab Initio Total-Energy Calculations Using a Plane-Wave Basis Set. *Phys. Rev. B* **1996**, *54*, 11169–11186.
- (41) Tran, F.; Blaha, P. Accurate Band Gaps of Semiconductors and Insulators with a Semilocal Exchange-Correlation Potential. *Phys. Rev. Lett.* **2009**, *102*, 226401.
- (42) Schwarz, K.; Blaha, P.; Madsen, G. Electronic Structure Calculations of Solids Using the WIEN2k Package for Material Sciences. *Comput. Phys. Commun.* **2002**, *147*, 71–76.
- (43) Paier, J.; Marsman, M.; Hummer, K.; Kresse, G. Screened Hybrid Density Functionals Applied to Solids. *J. Chem. Phys.* **2006**, *124*, 154709.
- (44) Hellman, O.; Abrikosov, I. A.; Simak, S. I. Lattice Dynamics of Anharmonic Solids from First Principles. *Phys. Rev. B* **2011**, *84*, 180301.
- (45) Li, W.; Carrete, J.; Nebil, A. K.; Natalio, M. ShengBTE: A Solver of the Boltzmann Transport Equation for Phonons. *Comput. Phys. Commun.* **2014**, *185*, 1747–1758.
- (46) Togo, A.; Tanaka, I. First Principles Phonon Calculations in Materials Science. *Scr. Mater.* **2015**, *108*, 1–5.
- (47) Li, W.; Lindsay, L.; Broido, D. A.; Stewart, D. A.; Mingo, N. Thermal Conductivity of Bulk and Nanowire $\text{Mg}_2\text{Si}_x\text{Sn}_{1-x}$ Alloys from First Principles. *Phys. Rev. B* **2012**, *86*, 174307.

- (48) Sieskind, M.; Polian, A.; Fischer, M.; Decremps, F. Some Scaling Factors of Physical Properties Dependent on Phonons in the Case of the Families of the Fluorite and of the Matlockite. *J. Phys. Chem. Solids* **1998**, *59*, 75–82.
- (49) Ji, H. S.; Togo, A.; Kaviani, M.; Tanaka, I.; Shim, J. H. Low Phonon Conductivity of Layered BiCuOS, BiCuOSe, and BiCuOTe from First Principles. *Phys. Rev. B* **2016**, *94*, 115203.
- (50) Biswas, R. K.; Pati, S. K. Vibrational Spectra of MO (M = Sn/Pb) in Their Bulk and Single-Layer Forms: Role of Avoided Crossing in Their Thermodynamic Properties. *Bull. Mater. Sci.* **2020**, *43*, 322.
- (51) Liu, B.; Shi, C.; Yin, M.; Fu, Y.; Shen, D. Electronic, Optical and Luminescent Properties of PbFCl Single Crystal. *J. Phys. Condens. Matter* **2005**, *17*, 5087–5094.
- (52) Reshak, A. H.; Charifi, Z.; Baaziz, H. First-Principles Study of the Optical Properties of PbFX (X = Cl, Br, I) Compounds in Its Matlockite-Type Structure. *Eur. Phys. J. B* **2007**, *60*, 463–468.
- (53) Haj Hassan, F. E.; Akbarzadeh, H.; Hashemifar, S.; Mokhtari, A. Structural and Electronic Properties of Matlockite MFX (M = Sr, Ba, Pb; X = Cl, Br, I) Compounds. *J. Phys. Chem. Solids* **2004**, *65*, 1871–1878.
- (54) Waghmare, U. V.; Spaldin, N. A.; Kandpal, H. C.; Seshadri, R. First-Principles Indicators of Metallicity and Cation Off-Centricity in the IV-VI Rocksalt Chalcogenides of Divalent Ge, Sn, and Pb. *Phys. Rev. B* **2003**, *67*, 125111.
- (55) Lv, Z.-L.; Cui, H.-L.; Li, X.-H.; Wang, H.; Ji, G.-F. First Principles Study of the Vibrational, Dielectric and Thermal Properties of SrClF. *Eur. Phys. J. B* **2017**, *90*, 57.

- (56) Sundarakannan, B.; Ravindran, T.; Kesavamoorthy, R.; Satyanarayana, S. High Pressure Raman Spectroscopic Study of BaFCl. *Solid State Commun.* **2002**, *124*, 385–389.
- (57) Sorb, Y. A.; Subramanian, N.; Ravindran, T. R. High Pressure Raman Spectroscopy of Layered Matlockite, PbFCl. *J. Phys. Condens. Matter* **2013**, *25*, 155401.
- (58) Kanchana, V.; Yedukondalu, N.; Vaitheeswaran, G. Lattice Dynamics and Electronic Structure of Mixed Halofluoride Scintillators Under High Pressure. *AIP Conf. Proc.* **2015**, *1665*, 090009.
- (59) Yedukondalu, N.; Vaitheeswaran, G. Vibrational Properties of BaClF, BaBrF and BaIF Under High Pressure. *J. Phys. Conf. Ser.* **2012**, *377*, 012070.
- (60) Rakesh Roshan, S. C.; Yedukondalu, N.; Muthaiah, R.; Lavanya, K.; Anees, P.; Kumar, R. R.; Rao, T. V.; Ehm, L.; Parise, J. B. Anomalous Lattice Thermal Conductivity in Rocksalt IIA-VIA Compounds. *ACS Appl. Energy Mater.* **2022**, *5*, 882–896.
- (61) Fan, D. D.; Liu, H. J.; Cheng, L.; Zhang, J.; Jiang, P. H.; Wei, J.; Liang, J. H.; Shi, J. Understanding the Electronic and Phonon Transport Properties of a Thermoelectric Material BiCuSeO: A First-Principles Study. *Phys. Chem. Chem. Phys.* **2017**, *19*, 12913–12920.
- (62) Xiao, Y.; Chang, C.; Pei, Y.; Wu, D.; Peng, K.; Zhou, X.; Gong, S.; He, J.; Zhang, Y.; Zeng, Z. et al. Origin of Low Thermal Conductivity in SnSe. *Phys. Rev. B* **2016**, *94*, 125203.
- (63) Mukhopadhyay, S.; Parker, D. S.; Sales, B. C.; Poretzky, A. A.; McGuire, M. A.; Lindsay, L. Two-Channel Model for Ultralow Thermal Conductivity of Crystalline Tl_3VSe_4 . *Science* **2018**, *360*, 1455–1458.
- (64) Mukhopadhyay, S.; Reinecke, T. L. Lone-Pair Electron-Driven Thermoelectrics at Room Temperature. *J. Phys. Chem. Lett.* **2019**, *10*, 4117–4122.

- (65) Wu, M.; Enamullah,; Huang, L. Unusual Lattice Thermal Conductivity in the Simple Crystalline Compounds TlXTe_2 ($X = \text{Ga}, \text{In}$). *Phys. Rev. B* **2019**, *100*, 075207.
- (66) Shafique, A.; Sharma, S.; Sajjad, M.; Schwingenschlögl, U. Multivalley Band Structure and Phonon-Glass Behavior of TlAgTe . *ACS Appl. Energy Mater.* **2021**, *4*, 2174–2180.
- (67) Kurosaki, K.; Goto, K.; Muta, H.; Yamanaka, S. Enhancement of Thermoelectric Figure of Merit of AgTlTe by Tuning the Carrier Concentration. *J. Appl. Phys.* **2007**, *102*, 023707.

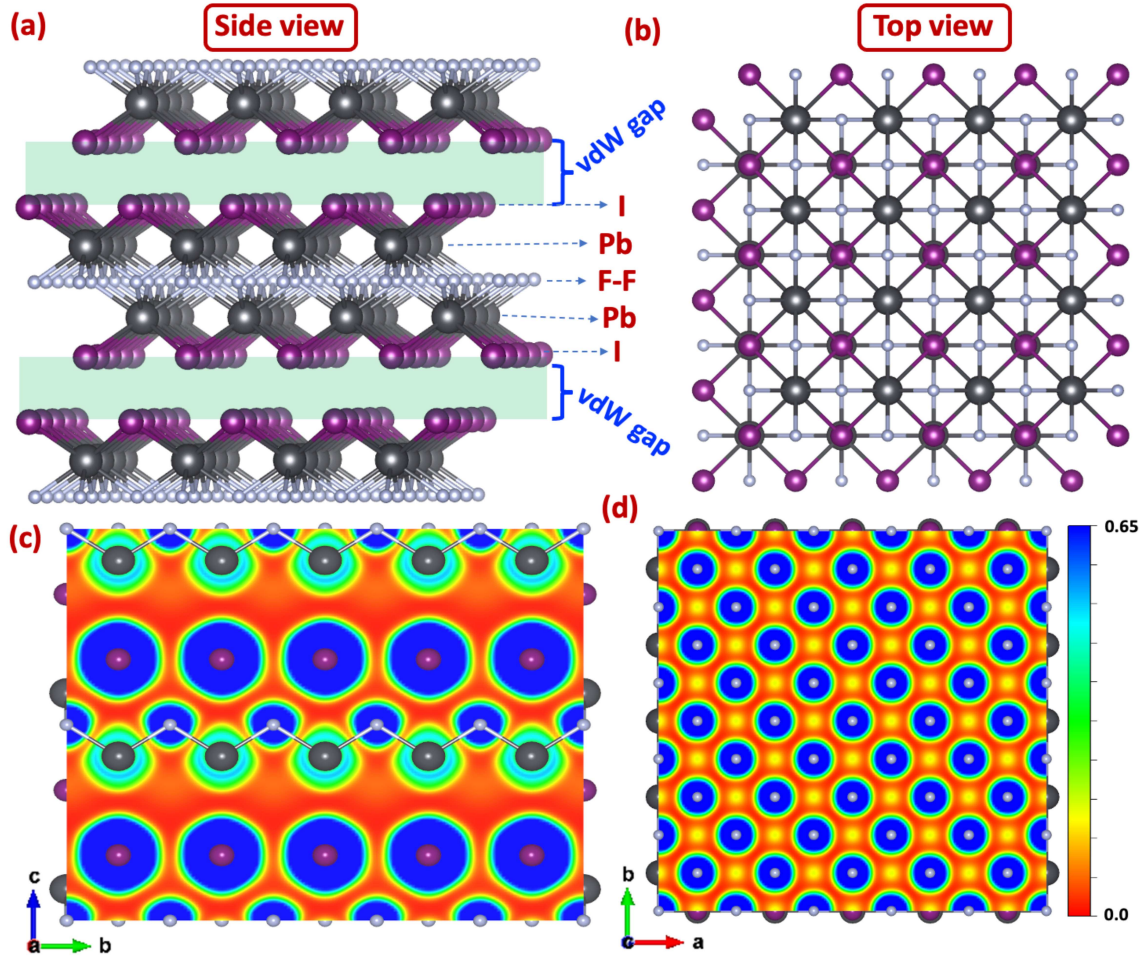
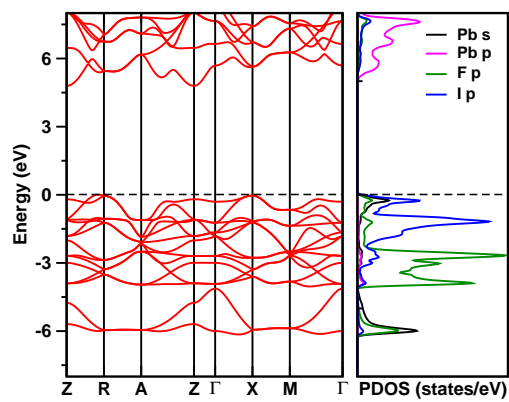
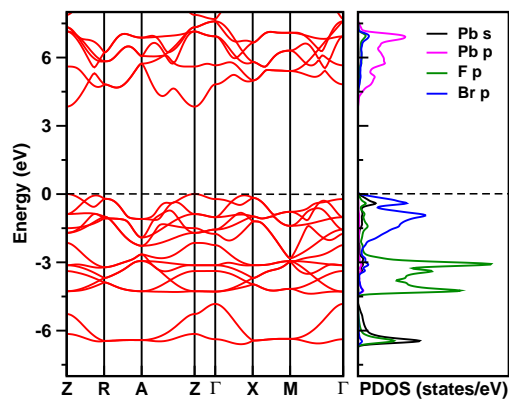


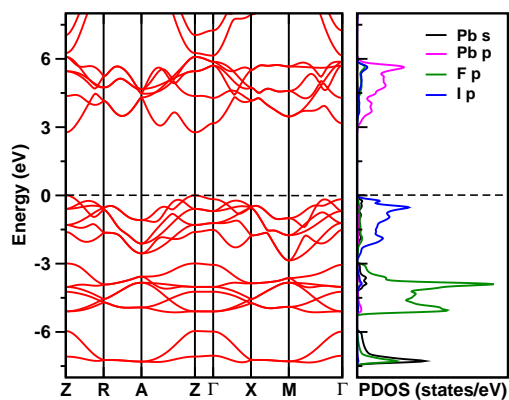
Figure 1: Layered crystal structure of PbIF in (a) side and (b) top views. ELF of PbIF in the (c) bc - and (d) ab -planes.



(a)

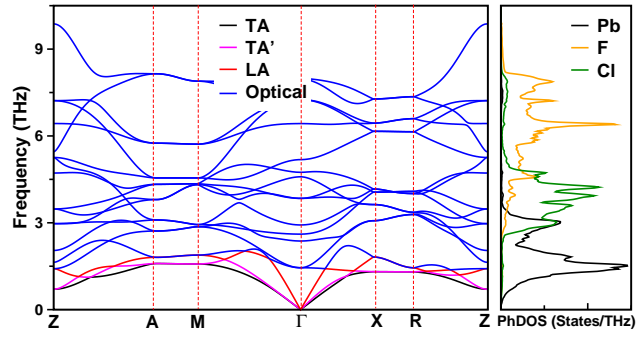


(b)

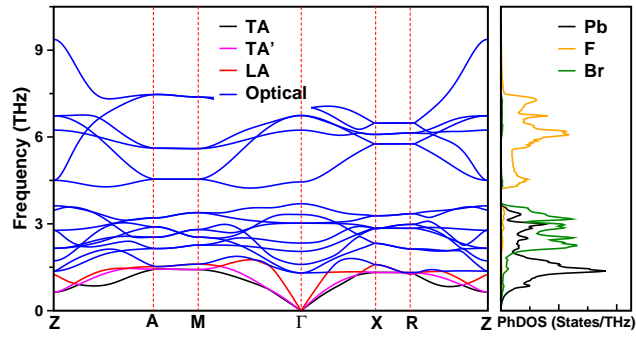


(c)

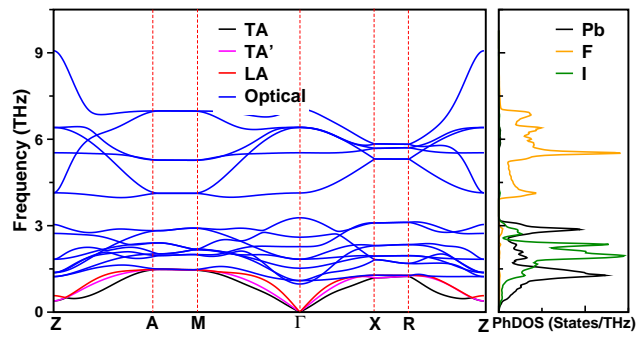
Figure 2: Electronic band structure and projected densities of states of (a) PbCIF, (b) PbBrF, and (c) PbIF taking into account the SOC.



(a)

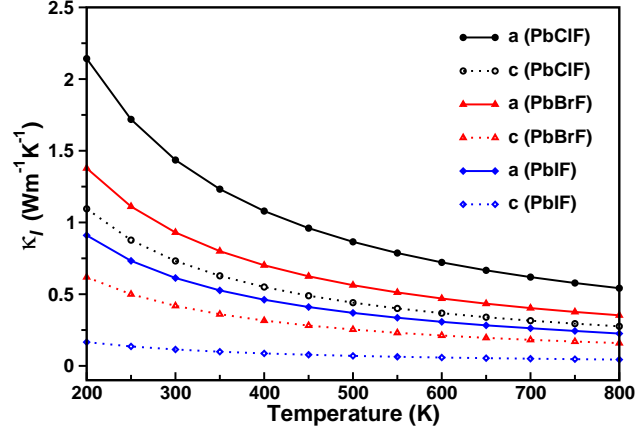


(b)

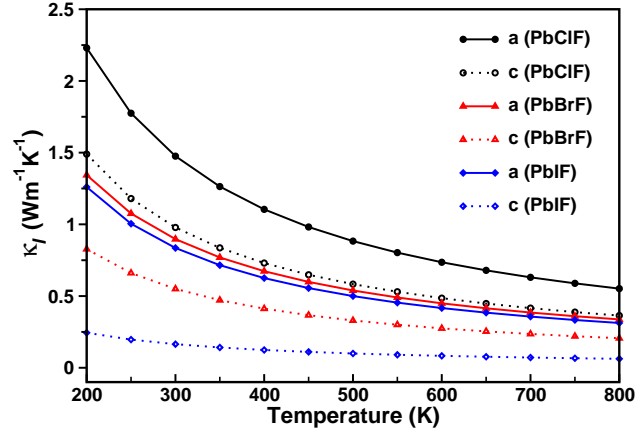


(c)

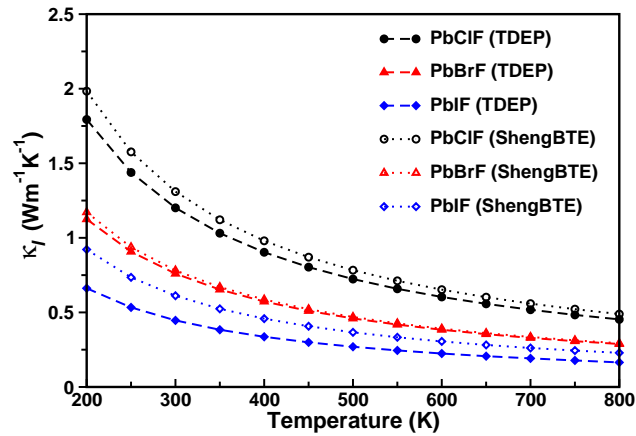
Figure 3: Phonon dispersion and projected phonon densities of states of (a) PbClF, (b) PbBrF, and (c) PbIF at 300 K.



(a)

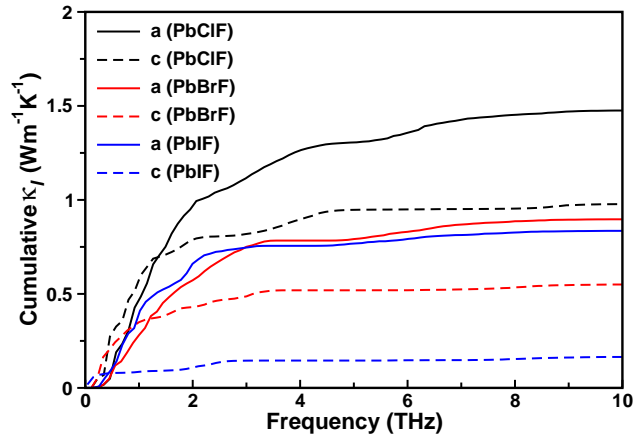


(b)

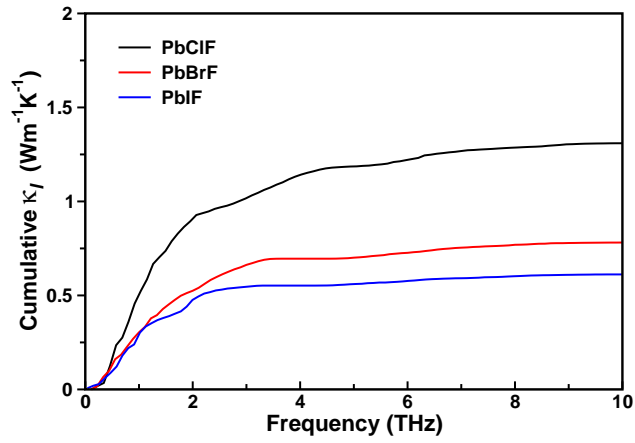


(c)

Figure 4: (a, b) Anisotropic and (c) average lattice thermal conductivities as functions of temperature for PbXF ($X = \text{Cl, Br, I}$) using TDEP and ShengBTE by solving the BTE iteratively.

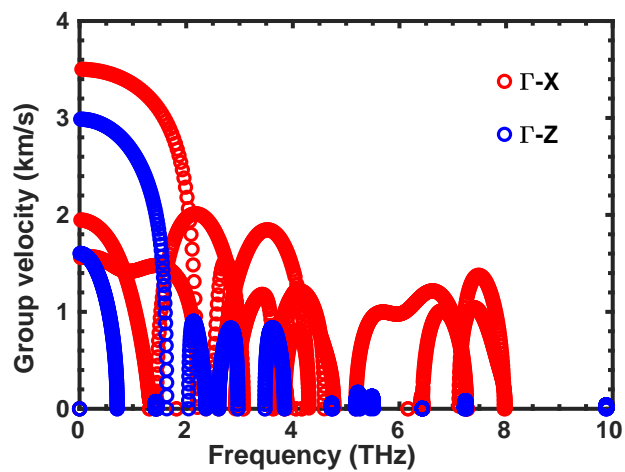


(a)

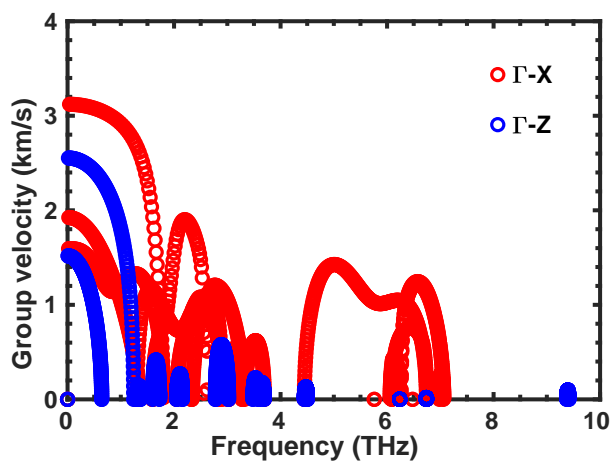


(b)

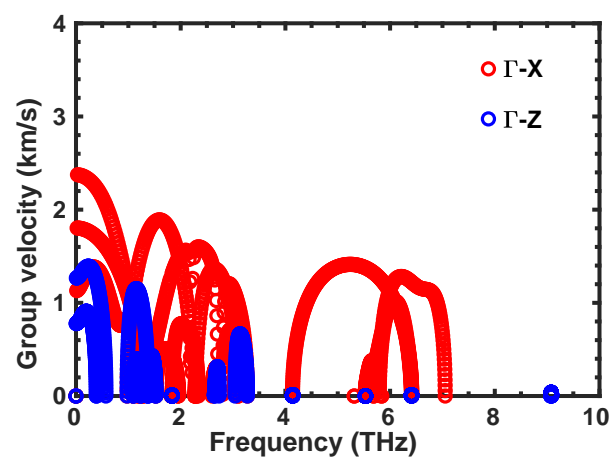
Figure 5: (a) Cumulative and (b) average cumulative lattice thermal conductivities of PbXF ($X = \text{Cl}, \text{Br}, \text{I}$) at 300 K.



(a)

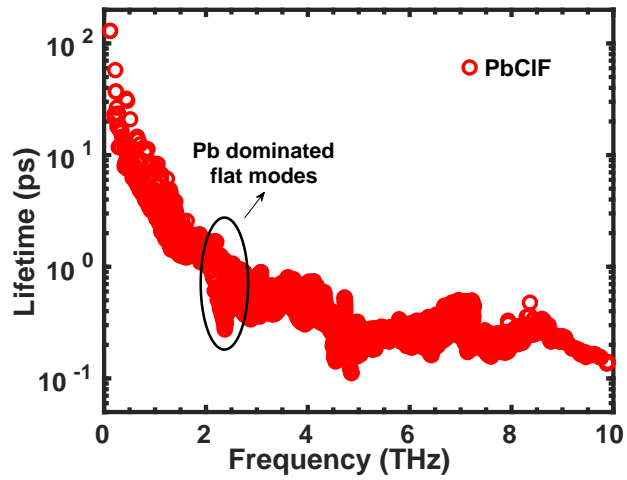


(b)

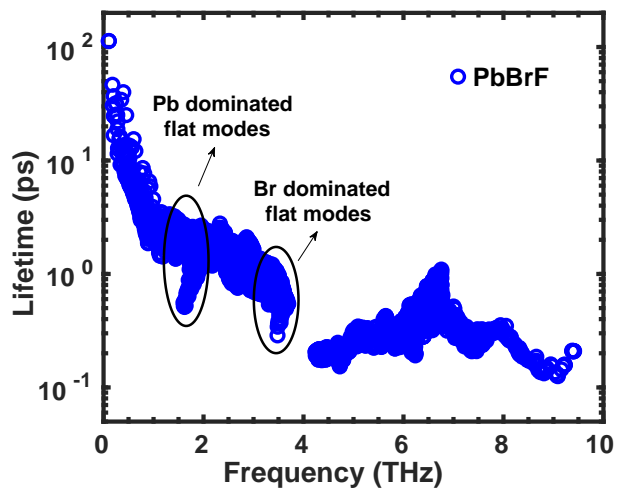


(c)

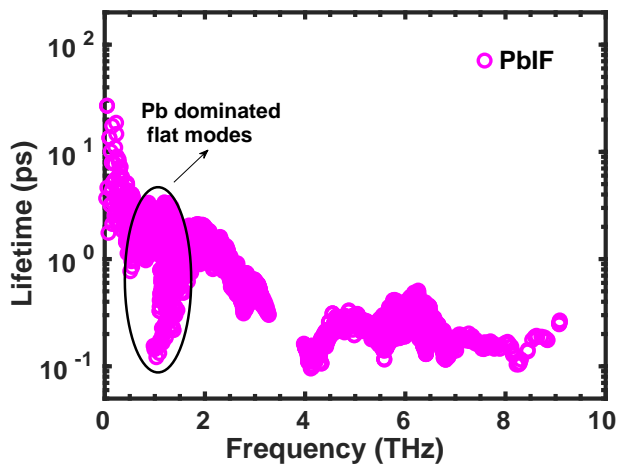
Figure 6: Phonon group velocities of (a) PbClF, (b) PbBrF, and (c) PbIF in the Γ -X and Γ -Z directions as functions of frequency.



(a)



(b)



(c)

Figure 7: Phonon lifetimes of (a) PbClF, (b) PbBrF, and (c) PbIF as functions of frequency.

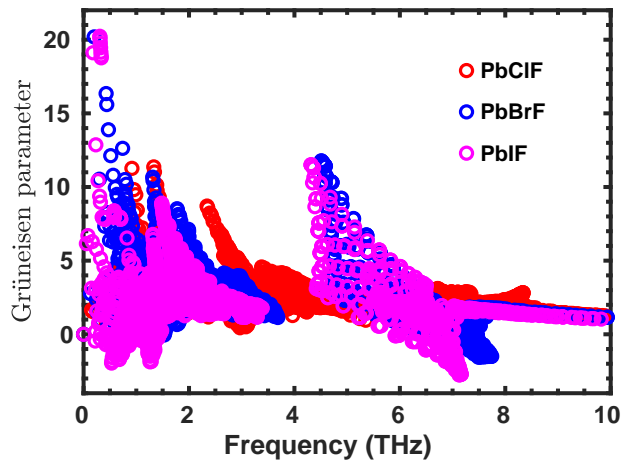


Figure 8: Grüneisen parameter of PbXF ($X = \text{Cl}, \text{Br}, \text{I}$) as a function of frequency.

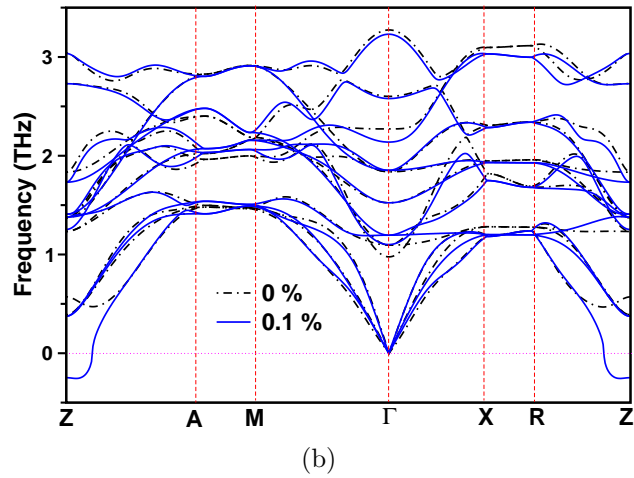
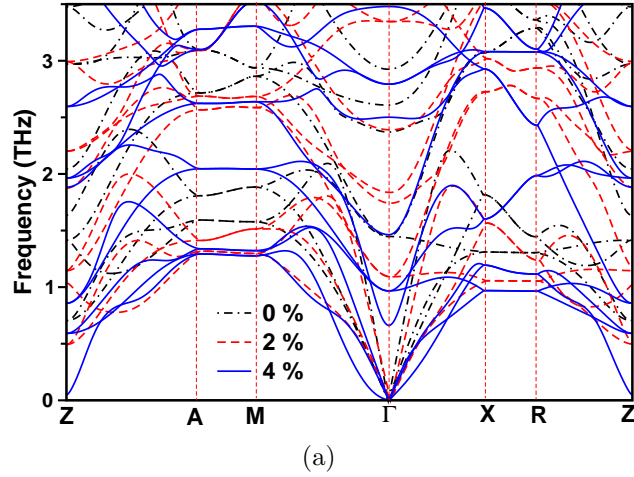
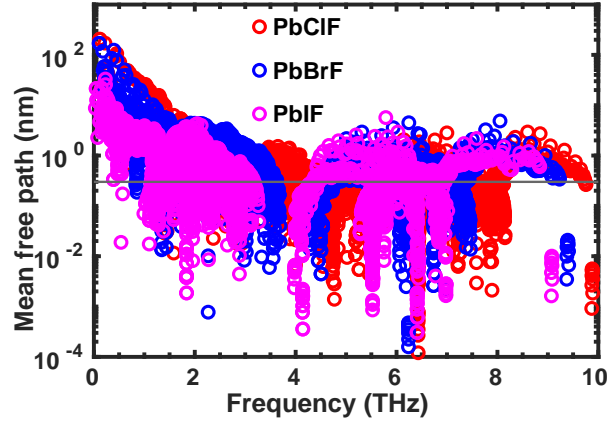
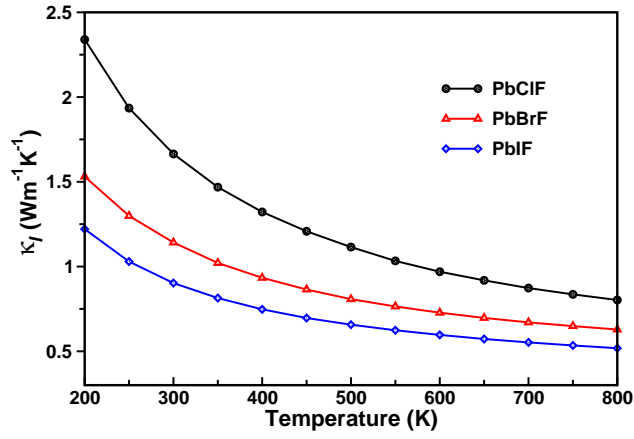


Figure 9: Phonon dispersion under volume expansion for (a) PbClF (0-4%) and (b) PbIF (0-0.1%) at 300 K. Soft phonon modes are observed in the Z-A and R-Z directions. A lattice instability is predicted for PbIF close to the equilibrium volume.



(a)



(b)

Figure 10: (a) Phonon mean free path as a function of frequency and (b) temperature dependence of the lattice thermal conductivity using the two channel transport model for PbXF ($X = \text{Cl}, \text{Br}, \text{I}$).

Table 1: Bader charges of the constituent elements of PbXF (X = Cl, Br, I).

Element	Formal charge	PbClF	PbBrF	PbIF
Pb	+2	+1.4	+1.4	+1.3
F	-1	-0.8	-0.8	-0.8
Cl/Br/I	-1	-0.7	-0.6	-0.5

Table 2: Second order elastic constants (in GPa) of PbXF (X = Cl, Br, I).

		C ₁₁	C ₃₃	C ₄₄	C ₆₆	C ₁₂	C ₁₃
PbClF	This work ^a	88	71	21	31	46	46
	This work ^b	80	56	18	26	40	39
	Others ^c	89	75	28	31	29	41
PbBrF	This work ^a	80	47	21	32	44	39
	This work ^b	74	36	19	26	39	34
	Others ^c	80	68	25	28	26	37
PbIF	This work ^a	60	15	10	23	22	15
	This work ^b	59	13	12	23	23	16
	Others ^c	67	56	21	23	21	30

^aAt the PBEsol equilibrium volume

^bAt the experimental volume

^cRef 48.

Table 3: Bulk modulus (B_V , B_R , B_{VRH} in GPa), shear modulus (G_V , G_R , G_{VRH} in GPa), Young's modulus (E in GPa), density (ρ in gr/cc), sound velocity (v_l , v_t , v_m in km/s), and Debye temperature (θ in K) of PbXF (X = Cl, Br, I).

	PbClF	PbBrF	PbIF
B_V	58.1	50.2	26.4
B_R	57.9	45.6	14.3
B_{VRH}	57.9	47.9	20.3
G_V	21.8	20.4	14.4
G_R	20.8	17.3	9.9
G_{VRH}	21.3	18.8	12.2
E	56.9	49.9	30.4
ρ	7.3	7.8	7.5
v_l	3.4	3.1	2.2
v_t	1.7	1.6	1.3
v_m	1.9	1.7	1.4
θ	210.7	185.7	142.1

Table 4: Born effective charge (Z^*), electronic dielectric constant (ϵ^∞), and ionic dielectric constant (ϵ^0) of PbXF ($X = \text{Cl, Br, I}$). The symbols \parallel and \perp represent the out-of-plane and in-plane directions, respectively.

	Atom	Z^*_{\parallel}	Z^*_{\perp}	$\epsilon^{\infty}_{\parallel}$ ($\epsilon^{\infty}_{\perp}$)	ϵ^0_{\parallel} (ϵ^0_{\perp})
PbClF	Pb	3.42	3.74	4.41 (5.00)	20.95 (38.36)
	Cl	-1.37	-1.99		
	F	-2.05	-1.76		
PbBrF	Pb	3.45	3.98	4.86 (5.88)	19.87 (42.57)
	Br	-1.22	-2.10		
	F	-2.22	-1.88		
PbIF	Pb	2.91	4.20	4.71 (6.73)	5.00 (41.37)
	I	-0.76	-2.17		
	F	-2.15	-2.03		

Table 5: Electronic band gaps (in eV) with and without SOC of PbXF ($X = \text{Cl, Br, I}$) using the PBE functional, HSE functional, and TB-mBJ potential compared with reflection spectrum measurements⁵¹ and calculations.

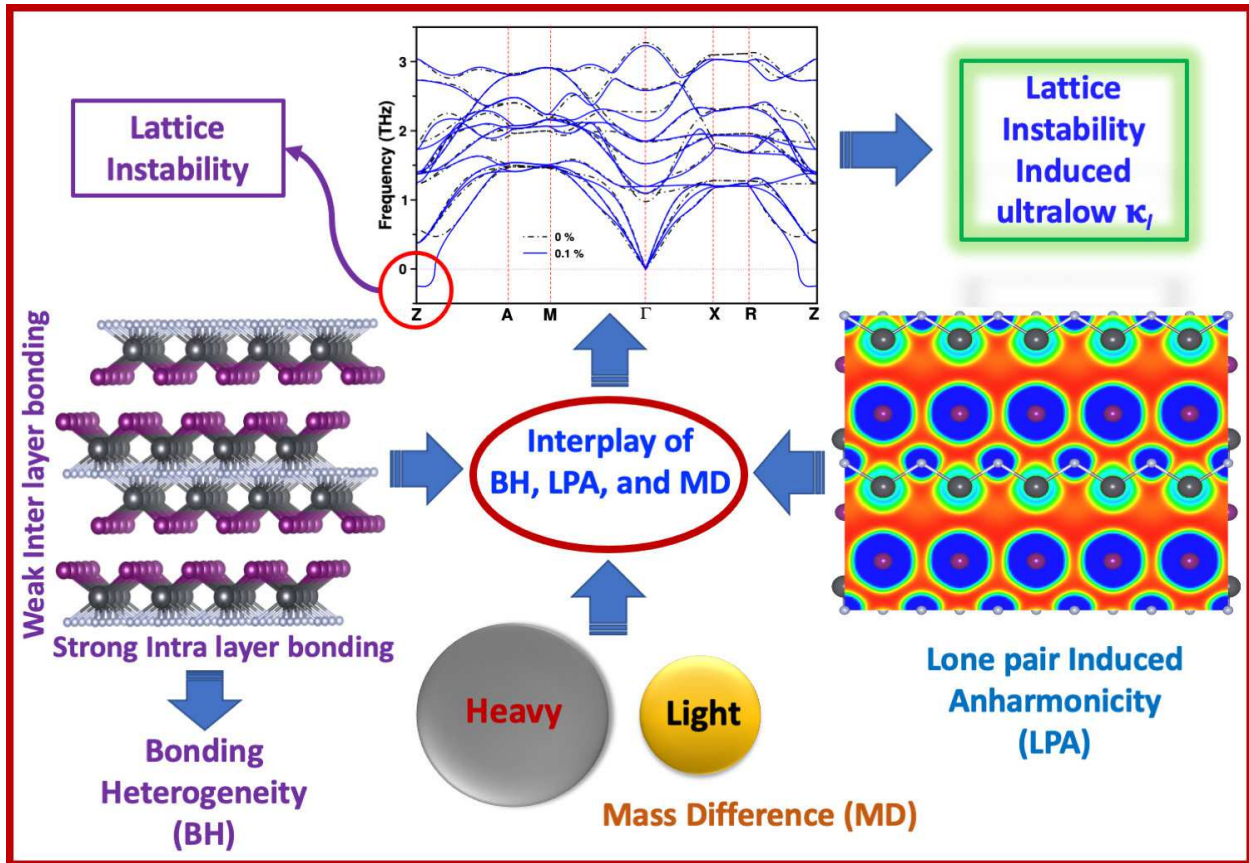
	Method	PbClF	PbBrF	PbIF
This work	PBE	3.5	2.6	1.8
	PBE+SOC	3.2	2.3	1.4
	TB-mBJ	4.8	3.9	2.8
	TB-mBJ+SOC	4.7	3.8	2.6
	HSE	4.8	4.0	3.6
	HSE+SOC	4.7	3.9	3.4
Others	LDA ^a	3.23	2.39	1.73
	PBE ^{a,b}	3.49, 3.5	2.63	2.0
	EV ^{a,c}	4.28, 4.32	3.31, 3.37	2.61, 2.48
	GW ^b	5.0	–	–
Experiment ^b		5.2	–	–

^aRef 53. ^bRef 51. ^cRef. 52.

Table 6: Phonon group velocities (in km/s) of the acoustic branches of PbXF ($X = \text{Cl, Br, I}$) in the Γ -X and Γ -Z directions.

		PbClF	PbBr	PbIF
Γ -X	TA1	1.56	1.59	1.13
	TA2	1.95	1.92	1.80
	LA	3.50	3.12	2.37
Γ -Z	TA1	1.60	1.52	0.78
	TA2	1.60	1.52	0.78
	LA	2.99	2.55	1.26

TOC Graphic



Interplay of bonding heterogeneity, lone-pair induced anharmonicity and constituent elements with high mass difference within the same crystal structure aid in designing ultralow κ_l materials for thermal energy management applications.

Supporting Information

Lattice Instability and Ultralow Lattice Thermal Conductivity of Layered PbIF

N. Yedukondalu,^{*,†,‡} Aamir Shafique,[¶] S. C. Rakesh Roshan,^{§,||} Mohamed Barhoumi,[⊥] Rajmohan Muthaiah,[#] Lars Ehm,^{†,‡} John B. Parise,^{†,‡} and Udo Schwingenschlögl^{*,¶}

[†]*Department of Geosciences, Stony Brook University, Stony Brook, New York 11794-2100, USA*

[‡]*Joint Photon Sciences Institute, Stony Brook University, Stony Brook, New York 11790-2100, USA*

[¶]*Applied Physics Program, Physical Science and Engineering Division (PSE), King Abdullah University of Science and Technology (KAUST), Thuwal 23955-6900, Saudi Arabia*

[§]*Rajiv Gandhi University of Knowledge Technologies, Basar, Telangana-504107, India*

^{||}*Department of Physics, National Institute of Technology-Warangal, Telangana, India*

[⊥]*Laboratoire de la Matière Condensée et des Nanosciences (LMCN), Université de Monastir, Département de Physique, Faculté des Sciences de Monastir, Avenue de le environnement, 5019 Monastir, Tunisia*

[#]*School of Aerospace and Mechanical Engineering, University of Oklahoma, Norman, OK 73019, USA*

E-mail: nykondalu@gmail.com; udo.schwingenschlogl@kaust.edu.sa

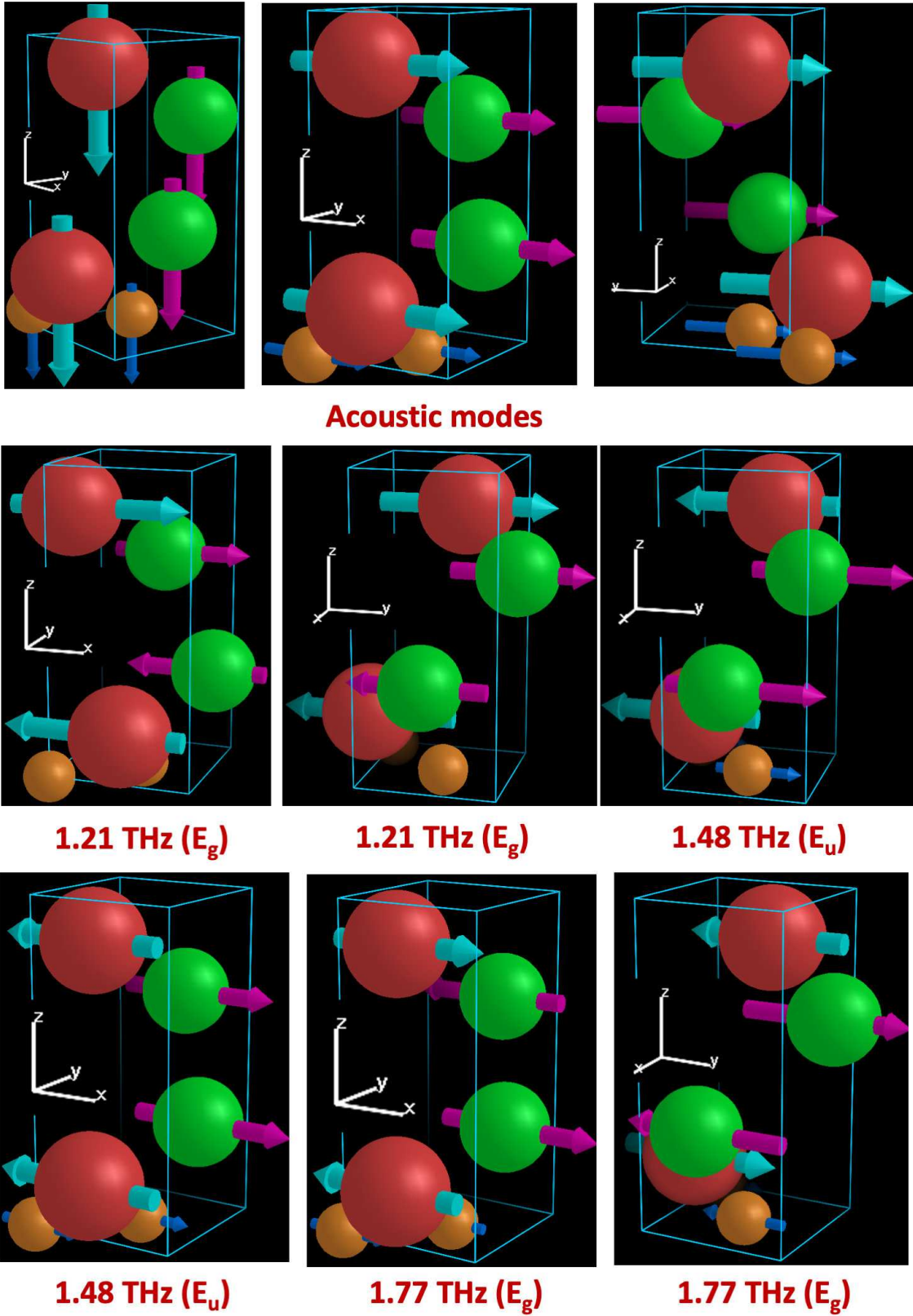


Figure S1: Eigenvectors of the acoustic and low frequency optical phonons of PbIF. E_g and E_u are doubly degenerate.

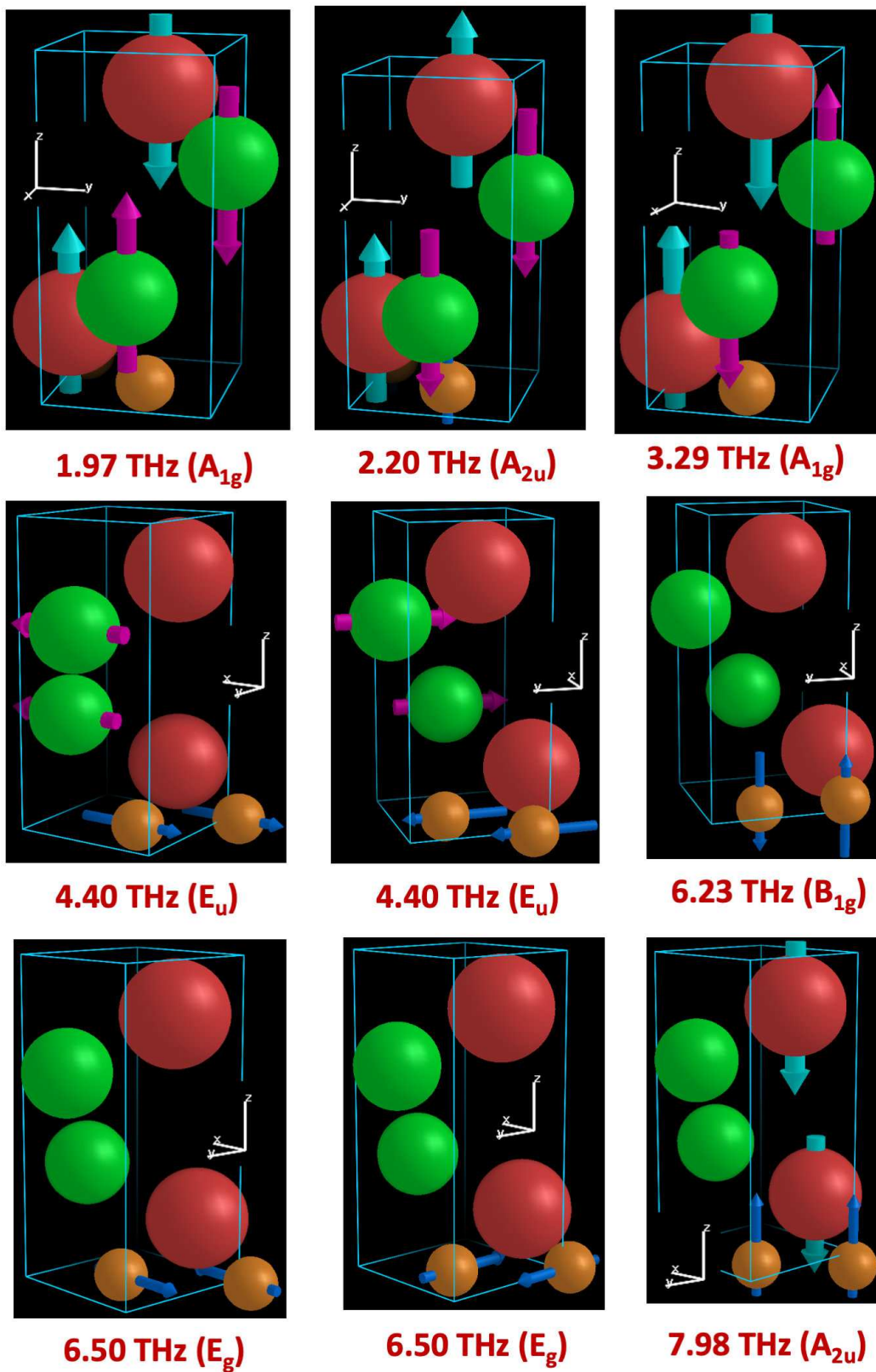


Figure S2: Eigenvectors of the intermediate and high frequency optical phonons of PbIF. E_g and E_u are doubly degenerate.

Table S1: Ground state lattice parameters (a, c in Å) and volume (V in Å³) of PbIF using standard and dispersion corrected DFT methods.

Material	Method	a	c	V
PbIF	PBEsol	4.161	9.058	156.83
	DFT-D2	4.248	8.580	105.33
	optB88-vdW	4.233	8.976	160.83
	optB86b-vdW	4.218	8.888	158.13
	Experiment ^a	4.23	8.77	156.92

^aRef [1].

Table S2: Ground state structural properties of PbXF (X = Cl, Br, I) using the PBEsol functional compared with X-ray diffraction data and other calculations.

Material	Method	a	c	V	v	u
PbClF	This work	4.066	7.186	118.80	0.2077	0.6468
	Experiment ^a	4.11	7.246	122.4	0.2058	0.6497
	Experiment ^b	4.1077	7.2282	121.968	-	-
	Others	4.163 ^c , 4.404 ^d	7.340 ^c , 7.079 ^d	-	0.2075 ^c , 0.191 ^d	0.6463 ^c , 0.66 ^d
		4.151 ^e	7.354 ^e	-	0.2075 ^e	0.6463 ^e
PbBrF	This work	4.146	7.541	129.62	0.194	0.647
	Experiment ^a	4.18	7.59	132.62	0.195	0.650
	Others	4.231 ^c , 4.451 ^d	7.760 ^c , 7.202 ^d	-	0.1945 ^c , 0.187 ^d	0.6469 ^c , 0.664 ^d ,
		4.232 ^e	7.70 ^e	-	0.1945 ^e	0.6469 ^e
PbIF	This work	4.161	9.058	156.83	0.161	0.666
	Experiment ^f	4.23	8.77	156.92	0.167	0.65
	Others	4.250 ^c , 4.248 ^e	9.152 ^c , 8.87 ^e	-	0.1666 ^c , 0.1665 ^e	0.6578 ^c , 0.6577 ^e

^aRef [2]. ^bRef [3]. ^cRef [4]. ^dRef [5]. ^eRef [6]. ^fRef [1].

References

- (1) Decremps, F.; Fischer, M.; Polian, A.; Itié, J. P.; Sieskind, M. Ionic Layered PbFCl-type Compounds Under High Pressure. *Phys. Rev. B* **1999**, *59*, 4011–4022.
- (2) Pasero, M.; Perchiazzi, N. Crystal Structure Refinement of Matlockite. *Mineralogical Magazine* **1996**, *60*, 833–836.
- (3) Manjunath, K.; Servottam, S.; Soni, A.; Rao, C. N. R. A Study of Two-Dimensional PbFCl and BaFCl. *Bull. Mater. Sci.* **2020**, *43*, 312.
- (4) Haj Hassan, F. E.; Akbarzadeh, H.; Hashemifar, S.; Mokhtari, A. Structural and Electronic Properties of Matlockite MFX ($M = \text{Sr, Ba, Pb}$; $X = \text{Cl, Br, I}$) Compounds. *J. Phys. Chem. Solids* **2004**, *65*, 1871–1878.
- (5) Mittal, R.; Chaplot, S. L.; Sen, A.; Achary, S. N.; Tyagi, A. K. Lattice Dynamics and Inelastic Neutron Scattering Studies of MFX ($M = \text{Ba, Sr, Pb}$; $X = \text{Cl, Br, I}$). *Phys. Rev. B* **2003**, *67*, 134303.
- (6) Reshak, A. H.; Charifi, Z.; Baaziz, H. First-Principles Study of the Optical Properties of PbFX ($X = \text{Cl, Br, I}$) Compounds in Its Matlockite-Type Structure. *Eur. Phys. J. B* **2007**, *60*, 463–468.